Article

A Stability Control Method to Maintain Synchronization Stability of Wind Generation under Weak Grid

Minhai Wu [1], Jun Zeng [1], Gengning Ying [1], Jidong Xu [1], Shuangfei Yang [2], Yuebin Zhou [2] and Junfeng Liu [3,*]

1   The School of Electric Power Engineering, South China University of Technology, Guangzhou 510640, China; minhaiwu@foxmail.com (M.W.); junzeng@scut.edu.cn (J.Z.); 202110182778@mail.scut.edu.cn (G.Y.); 202221014917@mail.scut.edu.cn (J.X.)
2   State Key Laboratory of HVDC, Electric Power Research Institute, China Southern Power Grid Co., Ltd., Guangzhou 510663, China; yangsf@csg.cn (S.Y.); zhouyb@csg.cn (Y.Z.)
3   The School of Automation Science and Engineering, South China University of Technology, Guangzhou 510640, China
*   Correspondence: jf.liu@connect.polyu.hk

Abstract: When wind generation systems operate under weak grid conditions, synchronization stability issues may arise, restricting the wind farms' power transfer capacity. This paper aims to address these challenges on the grid side. Firstly, a clear exposition of the coupling mechanism between the grid-connected inverters (GCI) of wind generations and the weak grid is provided. Then, an equivalent parallel compensation method integrated into the PLL to enhance synchronization stability is proposed. The method changes the reference of the PLL and equivalently parallels the virtual resistance with the grid impedance, which alters the strength of the grid. It reshapes the inverter qq-axis impedance at the impedance level. And the proper design of the virtual resistance will enhance the system's stability without compromising the dynamic performance of PLL. In addition, the proposed method is robust to the parameter changes of the grid-connected system and the grid impedance measurement error. Experimental results are presented to validate the effectiveness of the compensation method.

Keywords: wind generation; weak grid; synchronization stability; coupling mechanism; equivalent parallel compensation; stability analysis

1. Introduction

The development of wind generation has gained significant momentum as a solution to environmental pollution in recent years. Given the decentralized nature of wind resources, power plants are often situated in remote locales. And it relies on GCI to access the conventional grid.

However, employing PLL as synchronization units in wind generation systems can potentially introduce synchronization instability problems, particularly under weak grid conditions [1]. The sub-synchronous resonance (SSR) was observed in the Xinjiang Type-IV wind generation plant [2].

The impedance-based stability criterion combined with the generalized Nyquist criterion (GNC) is extensively adopted to address the synchronization instability issues [3]. The dq-frame impedance model of GCI is established in [4], and the qq-axis negative resistance is considered as the fundamental factor contributing to synchronization instability. Ref. [5] analyzes the PLL feedforward effect on the control of GCI and concludes that the PLL current feedforward effect has a more adverse impact on system stability. Ref. [6] simplifies the MIMO impedance model to the SISO model to assess the impacts on the synchronization stability of PLL, current control, voltage feedforward, and DC voltage controller. Additionally, ref. [7] derives a SISO impedance model related to the synchronization loop, with PLL

loop shaping employed to enhance stability. In [8], a *d*-axis current error is feedforward to current control to damp the resonance based on the steady-state relationship.

The stability improvement methods are proposed for both the motor side [9] and the grid side. On the grid side, the widely adopted method is a feedforward method to reshape the impedance characteristic [10].

Since the PLL is pivotal for synchronization, several studies have focused on modifying the PLL [11,12]. Recent efforts have predominantly focused on changing the PLL input. Ref. [13] enhances the passivity of a GCI by multiplying the output impedance phase regulator of normalized magnitude with the phase-locked loop inputs. Ref. [14] introduces a compensation frame to achieve current control by phase lag compensation, which is employed in PLL. By modifying the PLL input, ref. [15] introduces a series resistance in the grid impedance to increase damping in the studied system. However, this method entails a complex impedance model. Ref. [16] analogous to the back electromotive force observer in DC motor control, the input of the PLL is readjusted by state estimation.

Some of the literature achieves oscillation suppression by employing novel control methods. The literature [17] points out that the grid-forming control has more stability under weak grids compared to the grid-following control, but it will be a risk of instability under strong grids. Ref. [18] controls the GCI without adopting PLL implemented by the voltage-modulated direct power control. And it can also be utilized in weak grids by employing a band-pass filter [19]. The adaptive dual-mode control is suggested for oscillation suppression, i.e., current source mode under a weak grid and voltage source mode under a strong grid [20]. Ref. [21] proposes a grid voltage feedforward control strategy based on multi-objective objective constraint to broaden the adaptation range of the system to the grid impedance.

In addition, ref. [22] analyzes the stability range of PLL parameters under weak grid, finding suitable parameters by iterative adjustment method to enhance the power transfer capability. Ref. [23] concludes that the guideline that the PLL bandwidth should not exceed one-tenth of the current loop may not be applicable under weak grid. Ref. [24] proposes a control parameter design method considering the fluctuation of the grid impedance to improve the dynamic stability under weak grid. The supplementary damping controllers, such as TCSC, have also been adopted to damp the SSR of wind generations [25].

However, stability enhancement methods based on optimizing system parameters sacrifice the bandwidth of the PLL or current control, increasing the coupling between the current control and PLL. The supplementary damping controllers are limited in their promotion by their high cost and complex operation control modes. Therefore, optimizing the grid-side or motor-side control system for the studied system is more appropriate.

But the current study of the coupling mechanism of a grid-connected system is still incomplete, resulting in the existing stability control strategies mainly relying on feedforward compensation based on the *q*-axis voltage. And the compensation term is complicated. When the grid impedance changes and the parameter changes during the actual operation of the system, it brings new challenges for the stability control methods. Hence, there is a pressing need to introduce novel stability control methods derived from the coupling mechanism of grid-connected systems.

This article proposes an equivalent parallel resistance compensation method on the grid side employed in the PLL, which is based on comprehending the root of instability. The highlights are summarized as below:

(a)   A clear exposition of the coupling mechanism among the PLL, weak grid, and current control is provided, laying the groundwork for forthcoming stability enhancement techniques.

(b)   An equivalent parallel resistance compensation method integrated into PLL is proposed to improve synchronization stability. It reshapes the *qq*-axis impedance and will not decrease the dynamic performance of PLL with a proper design of virtual resistance.

(c)   The compensation method demonstrates robustness against system parameter variations and grid impedance measurement errors.

The subsequent sections are structured as follows: Section 2 derives the investigated system's impedance model and analyzes the coupling mechanism between the PLL, weak grid, and current control. Section 3 presents the proposed equivalent parallel resistance compensation method, including its design and performance analysis. Section 4 conducts the experimental verification. Section 5 concludes and outlines future work.

2. Impedance Model and Stability Analysis of the Grid-Connected System

2.1. Description and Model of System

Because the dynamic of the DC capacitor is slow, the motor side and the grid side are decoupled in type-IV wind generation. Thus, the rotor side is represented by DC-source. The topology is shown in Figure 1. Filter inductor L_f is utilized to filter the GCI output voltage V_{iabc} to PCC voltage V_{abc}. By controlling the dq-component (i_d^c, i_q^c) of the current I_{abc} and synchronizing with the voltage of PCC, the grid-following control based on PLL can be achieved. Table 1 lists the introduction and the value of system parameters. *SCR* is usually used to define the grid strength, and the equation of *SCR* can be expressed as:

$$SCR = \frac{3V_g^2}{Z_g S} \tag{1}$$

where V_g is the grid voltage magnitude, Z_g is the grid impedance, and S is the rated capacity of the grid-connected system. When $SCR > 3$, it is considered a strong grid; $2 < SCR < 3$, it is considered a weak grid; and $SCR < 2$, it is considered a very weak grid.
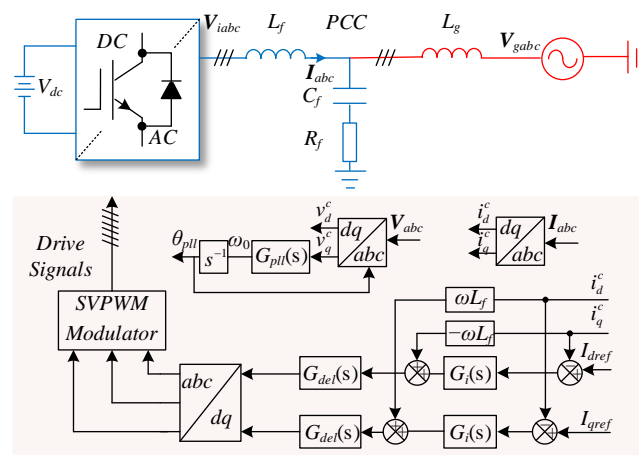

Figure 1. System topology and control diagram.

Table 1. System parameters.

Parameter	Values
DC-link voltage V_{dc}	400 V
Grid voltage RMS value V_g	130 V
Rated power P_n	2 kW
Filter inductors L_f	3 mH
Filter capacitors C_f	20 μF
Damping resistors R_f	10 Ω
Grid inductors L_g	9/16 mH
Switching frequency f_{sw}	10 kHz
Sampling frequency f_s	10 kHz
Proportional gain of G_i k_{pi}	5.24
Integral gain of G_i k_{ii}	1370
Proportional gain of G_{pll} k_{ppll}	4.2
Integral gain of G_{pll} k_{ipll}	384

The input of the PLL is V_{abc} rather than V_{gabc} under the weak grid case. This leads to distinct system frames and control frames. The dq-component of variables in the system and control frame are equal in steady state, namely $x_{dq}^s = x_{dq}^c$, where the control frame and the system frame are designated with "c" and "s".
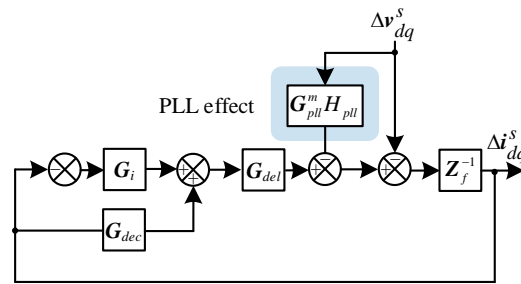
Figure 2a illustrates the control block of the GCI with PLL effects. The relationship between the current Δi_{dq} and modulated voltage Δe_{dq} in different frames is as follows [8]:

$$\Delta i_{dq}^c = \Delta i_{dq}^s + \underbrace{\begin{bmatrix} 0 & -I_{qref} \\ 0 & I_{dref} \end{bmatrix} H_{pll}(s) \Delta v_{dq}^s}_{G_{pll}^i(s)} \tag{2}$$

$$\Delta e_{dq}^c = \Delta e_{dq}^s + \underbrace{\begin{bmatrix} 0 & -V_{iq} \\ 0 & V_{id} \end{bmatrix} H_{pll}(s) \Delta v_{dq}^s}_{G_{pll}^v(s)} \tag{3}$$
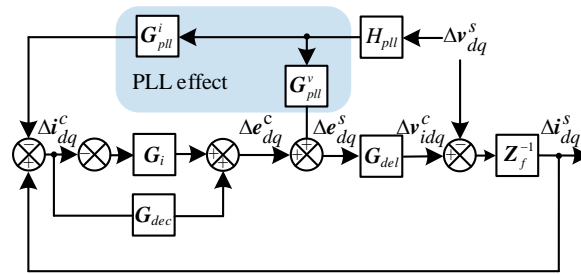
(a)

(b)

Figure 2. (**a**) Control block of GCI with PLL effects. (**b**) Equivalent diagram.

$G_{pll}^i(s)$ and $G_{pll}^v(s)$ represent the PLL feedforward effects on current and modulated voltage. I_{dqref} and V_{idq} denote the steady-state values [8]. $H_{pll}(s)$ describes the relationship from the Δv_q^s to the $\Delta \theta$:

$$H_{pll}(s) = \frac{G_{pll}(s)}{s + V_d^s G_{pll}(s)} \tag{4}$$

$$G_{pll}(s) = k_{ppll} + k_{ipll} \cdot s^{-1} \tag{5}$$

$G_i(s)$ represents the matrix of current control, $G_{dec}(s)$ is the matrix of decoupling term, and I is the unit matrix.

$$G_i(s) = Gi(s) \cdot I = \left(k_{pi} + k_{ii} \cdot s^{-1} \right) \cdot I \tag{6}$$

$$G_{dec}(s) = \begin{bmatrix} 0 & -\omega L_f \\ \omega L_f & 0 \end{bmatrix} \tag{7}$$

The impedance matrix $\mathbf{Z}_f$ corresponds to the inverter side filter inductance L_f and is expressed as:

$$\mathbf{Z}_f = \begin{bmatrix} sL_f & -\omega L_f \\ \omega L_f & sL_f \end{bmatrix} \tag{8}$$

The time delay matrix $\mathbf{G}_{del}(s)$ accounts for the digital control delay, with $T_{del} = 1.5\ T_s$. It is defined as:

$$\mathbf{G}_{del}(s) = \left(\frac{1 - 0.5T_{del} \cdot s}{1 + 0.5T_{del} \cdot s} \right) \cdot \mathbf{I} \tag{9}$$

Figure 2a can be further converted to Figure 2b, where $\mathbf{G}_{pll}^m(s)$ can be given by:

$$\mathbf{G}_{pll}^m = \mathbf{G}_{del}((\mathbf{G}_i - \mathbf{G}_{dec})\mathbf{G}_{pll}^i - \mathbf{G}_{pll}^v) \tag{10}$$

Considering that the capacitor branch has a more significant influence on the high-frequency dynamics, while the oscillation of the studied system primarily occurs at frequencies less than 200 Hz, the filter capacitor branch is simplified. Consequently, the expression for the inverter impedance $\mathbf{Z}_{out}$ can be obtained as:

$$\mathbf{Z}_{out} = \begin{bmatrix} Z_{out,dd} & Z_{out,dd} \\ Z_{out,qd} & Z_{out,qq} \end{bmatrix} = (\mathbf{Z}_f + (\mathbf{G}_i - \mathbf{G}_{dec})\mathbf{G}_{del}) \cdot (\mathbf{I} + \mathbf{G}_{pll}^m H_{pll})^{-1} \tag{11}$$

The grid impedance, denoted as $\mathbf{Z}_g$, can be obtained as follows:

$$\mathbf{Z}_g = \begin{bmatrix} sL_g & -\omega L_g \\ \omega L_g & sL_g \end{bmatrix} \tag{12}$$

2.2. Stability and the Coupling Mechanism Analysis

Based on (8), the $\mathbf{Z}_{out}$ can be presented in a more intuitive way:

$$\mathbf{Z}_{out} = (\underbrace{\mathbf{I} \cdot (\mathbf{Z}_f + (\mathbf{G}_i - \mathbf{G}_{dec})\mathbf{G}_{del})^{-1}}_{\mathbf{Z}_{plant}^{-1}} + \underbrace{\mathbf{G}_{pll}^m H_{pll} \cdot (\mathbf{Z}_f + (\mathbf{G}_i - \mathbf{G}_{dec})\mathbf{G}_{del})^{-1}}_{\mathbf{Z}_{pll}^{m\ -1}})^{-1} \tag{13}$$

$\mathbf{Z}_{out}$ denotes the impedance of the GCI incorporating the PLL feedforward effect, while $\mathbf{Z}_{plant}$ refers to the GCI impedance when the PLL feedforward path is not taken into account. $\mathbf{Z}_{pll}^m(s)$ represents the impedance formulated by the feedforward effect.

Figure 3 shows the GNC plot of the $\mathbf{L}_p(s) = \mathbf{Z}_g \cdot \mathbf{Z}_{plant}^{-1}$ when $L_g = 16$ mH and the $\mathbf{L}_o(s) = \mathbf{Z}_g \cdot \mathbf{Z}_{out}^{-1}$ when $L_g = 9$ mH, $L_g = 16$ mH. The eigen-traces λ_{1p}, λ_{2p} correspond to $\mathbf{L}_p(s)$, and the eigen-traces λ_{1o}, λ_{2o} correspond to $\mathbf{L}_o(s)$.
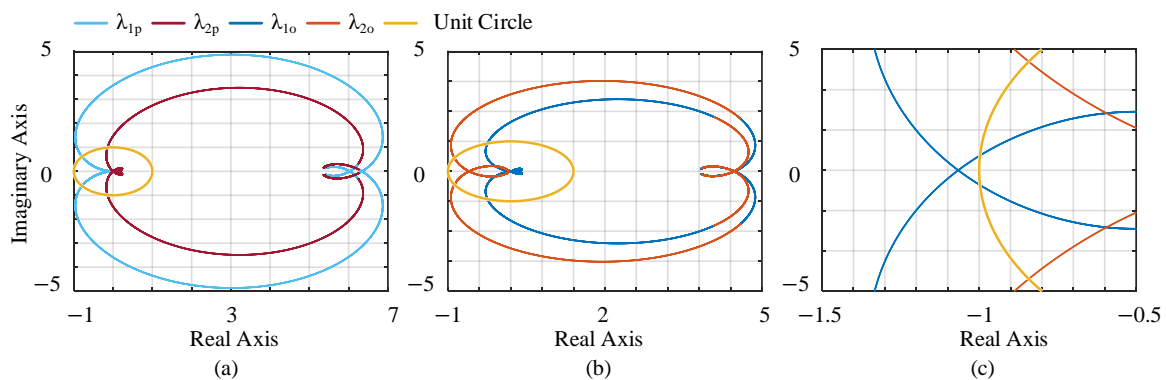
Figure 3. The GNC plot under weak grid (**a**) $L_g = 16$ mH, without PLL effect (**b**) $L_g = 9$ mH, with PLL effect (**c**) $L_g = 16$ mH, with PLL effect.

As depicted in Figure 3, when the PLL effect is not taken into account, and L_g = 16 mH, the λ_{1p}, λ_{2p} do not intersect $(-1, j0)$, where the stable operation can be maintained. When taking into account the PLL effect, it is evident that the system remains stable when L_g = 9 mH, whereas instability arises when L_g = 16 mH. Therefore, the system's stability is primarily influenced by both the PLL and the grid impedance. The coupling between the weak grid and the PLL will be explored in the following.

The Bode plot of the GCI impedance in *qq*-axis when considering PLL effects and not considering PLL effects is shown in Figure 4. It can be deduced that $\boldsymbol{Z}_{out,qq}$ exhibits capacitive impedance characteristics in *qq*-axis due to the PLL effect, which may couple with a weak grid and further contribute to instability. Thus, the PLL affects the stability of the studied system via current control by the feedforward effect.
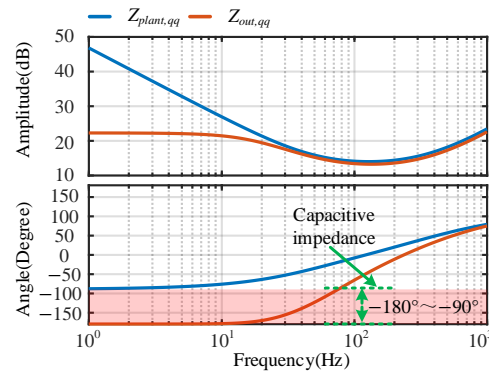

Figure 4. Bode plot of GCI impedance in *qq*-axis.

Further exploration of the coupling between the weak grid and PLL will be conducted subsequently. The steady-state relationship between the v_{dq}^s, v_{gdq}^s and $\boldsymbol{Z}_g$ can be formulated as:

$$v_{dq}^s = v_{gdq}^s + \boldsymbol{Z}_g \cdot i_{dq}^s \tag{14}$$

Linearizing Formula (14) and assuming negligible variation in the grid voltage v_{gdq}^s at steady state:

$$\Delta v_{dq}^s = \boldsymbol{Z}_g \cdot \Delta i_{dq}^s \tag{15}$$

Based on Formula (15), the small signal model of the PLL can be represented in Figure 5a. This depiction clearly reveals the interconnection between the $\boldsymbol{Z}_g$ and PLL. PLL further feedforwards the current control, resulting in the formulation of the *qq*-axis capacitive impedance area.

(a)

(b)
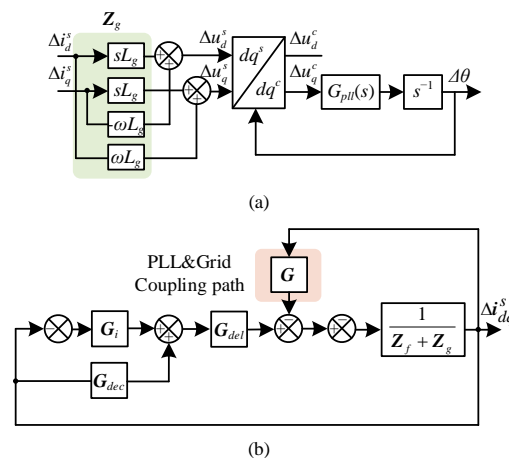
Figure 5. (**a**) PLL considering grid impedance (**b**) current control of GCI with PLL effects considering grid impedance.

Figure 5b further provides an intuitive representation of the coupling, where $\boldsymbol{G}$ denotes the coupling term, which can be mathematically obtained as:

$$\boldsymbol{G} = \boldsymbol{G}_{pll}^{m} H_{pll} \boldsymbol{Z}_g \tag{16}$$

3. Analysis and Design of Equivalent Parallel Compensation Method

3.1. Analysis of the Equivalent Parallel Compensation Method

When a virtual resistance is parallel with $\boldsymbol{Z}_g$, it leads to a modification in the reference of the PLL, consequently changing the coupling method. It results in a reduction in the coupling degree between the qq-axis capacitive impedance of the GCI and the inductive weak grid. Meanwhile, the damping of the studied system can be improved by the virtual resistance.

To achieve the stability control of the grid-connected system, an equivalent parallel compensation method integrated into PLL is proposed. The $\boldsymbol{Z}_g$ in complex space is expressed as follows [26]:

$$\boldsymbol{Z}_g = (s + j\omega_1)L_g \tag{17}$$

Assuming the virtual resistance R_v is parallel with $\boldsymbol{Z}_g$, the expression for the grid impedance $\boldsymbol{Z}_{g,com}$ after parallel connection can be expressed as:

$$\boldsymbol{Z}_{g,com} = \underbrace{\frac{R_v}{(s + j\omega_1)L_{mg} + R_v}}_{G_{vr,dq}}(s + j\omega_1)L_g \tag{18}$$

where L_{mg} is the grid impedance value measured by the impedance measuring device, $\boldsymbol{G}$ can be expressed as another expression:

$$\boldsymbol{G}(s) = \frac{\boldsymbol{G}_{pll}^{m}(s)}{H_{pll}(s)} \cdot \underbrace{G_{vr,dq} \cdot H_{pll}(s)}_{H_{pll,com}} \cdot (s + j\omega_1) \cdot L_g \tag{19}$$

The specific implementation of the virtual resistance will be discussed below. Due to the difficulty of paralleling the resistance with the grid impedance in practical applications, it can modify H_{pll} to $H_{pll,com}$, namely modify the input of the PLL as shown in Formula (18). Where $G_{vr,dq}$ in dq domain can be converted to $G_{vr,\alpha\beta}$ in $\alpha\beta$ domain:

$$G_{vr,\alpha\beta}(s) = e^{-j\theta}G_{vr,dq}(s + j\omega)e^{j\theta} = \frac{R_v}{sL_{mg} + R_v} \tag{20}$$

According to Formula (19), when multiplying the transfer function $G_{vr,\alpha\beta}$ with the PLL input in the $\alpha\beta$ domain, the transfer function of H_{pll} becomes $H_{pll,com}$, which equivalently parallels the virtual resistance R_v with the grid impedance. The equivalent parallel resistance compensation method alters the coupling method in the studied system. Adopting the equivalent parallel resistance compensation method, the coupling degree will decrease, which theoretically improves the damping of the studied system.

Expanding on the above analysis, the modified PLL structure is shown in Figure 6. Here, $\boldsymbol{G}_{vr,\alpha\beta} = G_{vr,\alpha\beta} \cdot \boldsymbol{I}$, and $\boldsymbol{G}_{bpf} = G_{bpf} \cdot \boldsymbol{I}$. G_{bpf} is the band-pass filter aimed at preserving high-frequency characteristics and suppressing additional harmonics, expressed as:

$$G_{bpf}(s) = \frac{2\xi\omega_1 s}{s^2 + 2\xi\omega_1 s + \omega_1{}^2} \tag{21}$$

where $\xi = 0.707$, ω_1 denotes the grid angular frequency. The introduction of $\boldsymbol{G}_{vr,\alpha\beta}$ changes the phase reference of PLL input, consequently altering the stable operational point. This

leads to an undesirable reactive power. Therefore, the *dq* transform angle should be modified, formulated as:

$$T_{\alpha\beta,dq} = e^{j\theta_{pll,com}} = \begin{bmatrix} \cos(\theta_{pll,com}) & -\sin(\theta_{pll,com}) \\ \sin(\theta_{pll,com}) & \cos(\theta_{pll,com}) \end{bmatrix} \tag{22}$$

where $\theta_{pll,com}$ represents the corrected *dq* transform angle. Since the phase shift of the G_{bpf} is 0 at the fundamental frequency, $\theta_{pll,com}$ can be formulated as:

$$\theta_{pll,com} = -\angle G_{vr,\alpha\beta} + \theta_{pll} \tag{23}$$
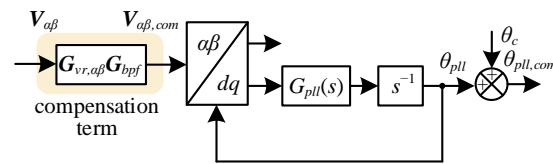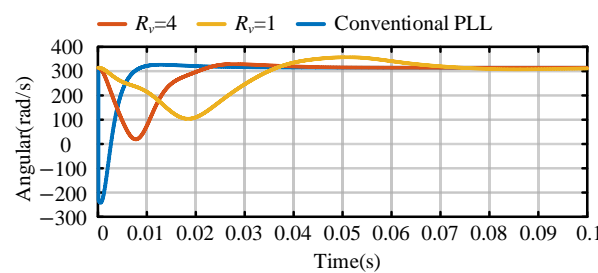

Figure 6. The improved PLL.

Consequently, the impedance of GCI with the proposed compensation method can be modified as follows:

$$Z_{out,com} = (Z_f + (G_i + G_{com})G_{del}) \cdot (I + G_{pll}^m G_{vr,dq} H_{pll})^{-1} \tag{24}$$

3.2. Dynamic Performance of Compensation Method

The compensation method is utilized in the PLL without impacting the current tracking dynamic performance. The impact of the compensation method on PLL dynamic performance is assessed through MATLAB R2021b/Simulink.

The dynamic performance of the frequency tracking for both the conventional PLL and the improved PLL with different values of R_v (R_v = 4 and R_v = 1) is illustrated in Figure 7. The improved PLL exhibits reduced undershoot compared to the conventional PLL. Furthermore, as R_v decreases, the undershoot is further minimized. Therefore, the improved PLL effectively mitigates the overshoot and undershoot observed in the conventional PLL.


Figure 7. Dynamic tracking frequency comparison between the improved PLL and the conventional PLL.

The dynamic response time is slightly changed with the improved PLL when R_v = 4. But it will further decrease with improved PLL when R_v = 1. Thus, the R_v will not be designed too small for a better dynamic response time of the PLL.

Thus, with a well-designed R_v, the proposed compensation method effectively maintains the stability while preserving minimal impact on the dynamic performance of the frequency tracking. For the selection of R_v, if R_v is too high, the coupling degree cannot be decreased. Conversely, if R_v is set too low, it may adversely affect the dynamic performance of the PLL.

3.3. Design and Stability Analysis

The stable range of the R_v is (0, 6) by employing the GNC to $L_c(s) = \mathbf{Z}_g \cdot \mathbf{Z}_{out,com}^{-1}$. In this study, R_v is chosen as 2, as it offers appropriate damping while preserving the dynamic performance of the PLL. Figure 8 illustrates the GNC plot for L_g = 16 mH and R_v = 2. The GNC plot clearly indicates that $(-1, j0)$ lies outside the λ_{1oc}, λ_{2oc}, indicating the stable operation of the interconnection system.
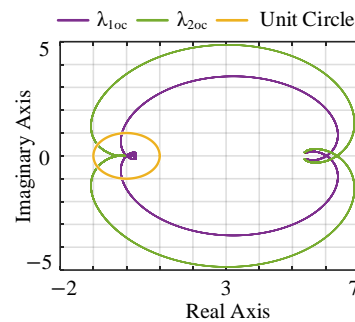
Figure 8. The GNC plot with proposed compensation method when L_g = 16 mH.

Figure 9 showcases the Bode plots of the GCI output impedance with and without compensation. Because the magnitude of the dq-axis impedance and the qd-axis impedance are relatively small, which can be omitted. The primary influence of the compensation method is located on the qq-axis impedance. With the implementation of the compensation method, the positive resistance area of qq-axis impedance expands. This signifies a reduction in the coupling degree between the PLL and the weak grid.
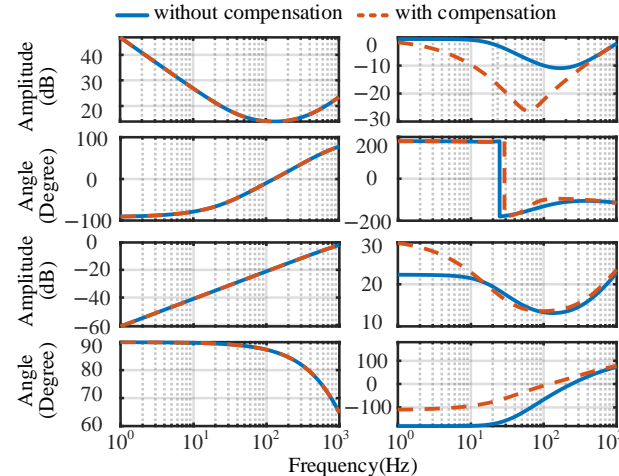
Figure 9. The Bode plot of GCI output impedance with and without compensation.

3.4. Robustness Analysis

The different operation modes of the grid-connected system may further decrease the stability. Factors such as the introduction of reactive power, increased PLL bandwidth, and grid impedance variations can destabilize the system. The errors of the estimated grid impedance L_{mg} of $G_{vr,dq}$ also influence the effect of the compensation method. Therefore, it is imperative to conduct further analysis on the robustness of the proposed compensation method.

To validate the robustness of the equivalent parallel resistance compensation method, a series of test cases listed in Table 2 were investigated. Depicted in Figure 10, the grid-connected system exhibited instability under cases I, II, and III. However, with the equivalent parallel resistance compensation method, stability was achieved in the grid-connected

system for all three cases. It demonstrates the robustness of the equivalent parallel resistance compensation in accommodating reactive power introduction, fluctuations in PLL bandwidth, and grid impedance.

Table 2. Test cases.

Cases	L_{mg} (mH)	L_g (mH)	PLL Parameters	dq-Axis Current (A)
I	16	16	$k_{ppll} = 4.2, k_{ipll} = 384$	$I_{dref} = 10, I_{qref} = 2$
II	16	16	$k_{ppll} = 4.2, k_{ipll} = 484$	$I_{dref} = 10, I_{qref} = 0$
III	16	17.5	$k_{ppll} = 4.2, k_{ipll} = 384$	$I_{dref} = 10, I_{qref} = 0$
IV	4.8 ($-70\% L_g$)	16	$k_{ppll} = 4.2, k_{ipll} = 384$	$I_{dref} = 10, I_{qref} = 0$
V	41.6 ($+160\% L_g$)	16	$k_{ppll} = 4.2, k_{ipll} = 384$	$I_{dref} = 10, I_{qref} = 0$
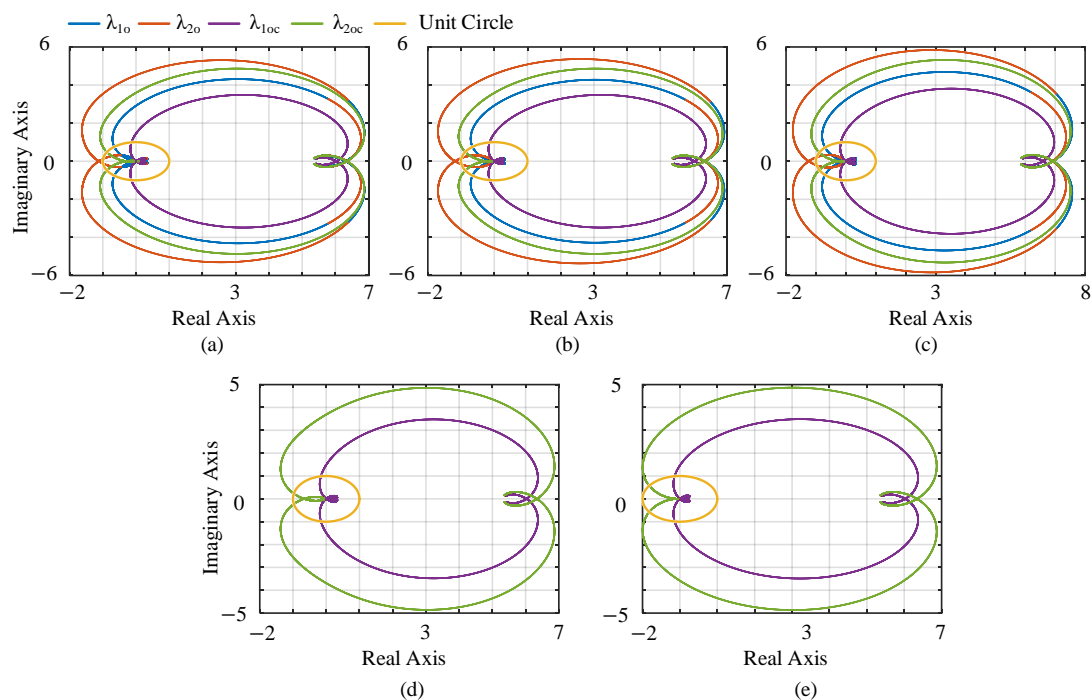
Figure 10. The GNC plot under $R_v = 2$ (**a**) case I; (**b**) case II; (**c**) case III; (**d**) case IV; (**e**) case V.

The proposed compensation method relies on obtaining grid impedance information. However, in practice, the unavoidable error of the grid impedance measurement device will lead to a deviation between the L_{mg} and the L_g. Therefore, it is necessary to analyze whether the equivalent parallel resistance compensation can achieve stable control when there are errors in grid impedance measurement.

The impacts of grid impedance estimation value L_{mg}, as revealed by Equation (19), on the compensation method can be inferred. Case IV and case V demonstrate that the compensation method can maintain stability even when the error in grid impedance measurement reaches $-70\% L_g$ and $+160 L_g$.

Compared with [27], the proposed compensation method is highly tolerated for grid impedance measurement errors. In addition, compared with the series resistance compensation method in [15], the impedance model of the proposed compensation method is not complicated.

4. Experiment and Simulation Verification

To verify the proposed equivalent parallel compensation method, a 2 kW grid-connected system is built up, employing a PM50CLA20 inverter made by Mitsubishi in Tokyo, Japan, and YXSPACE-SP2000 made by YANXU in Nanjing, China. Additionally, IT6535C serves

as the DC power source, which is made by ITCH in Nanjing, China. And GCT33060 functions as the grid simulator, which is made by HANSUN in Shanghai, China. The weak grid is realized by connecting the inductor between the converter and grid simulator. The experimental setup is depicted in Figure 11.
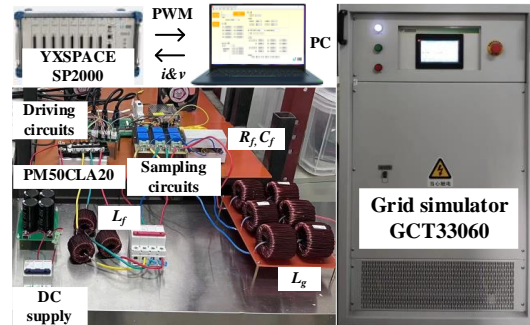

Figure 11. Experimental setup.

Figure 12 shows the waveforms with different L_g. It can be observed from Figure 12b that when the SCR is switched from 4.6 to 2.59, the oscillations will occur. Notably, a positive-sequence frequency of 111.25 Hz and a negative-sequence frequency of 11.25 Hz are observed due to the mirror frequency effect, as illustrated in Figure 12c.
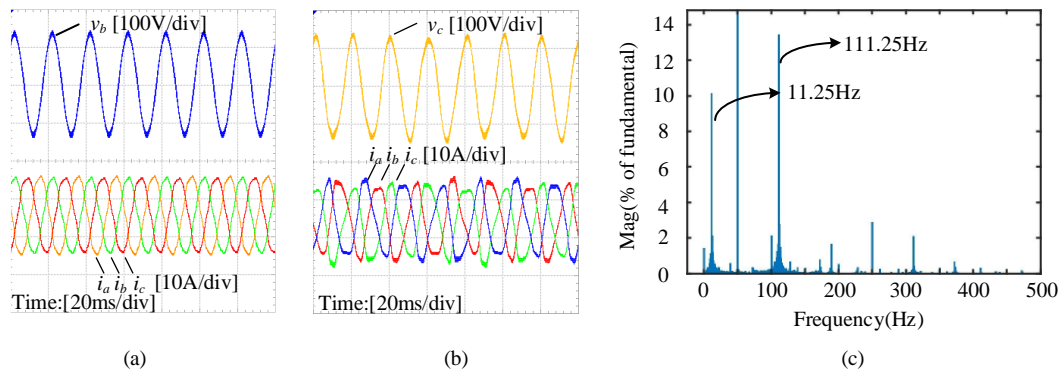

Figure 12. Waveforms under (**a**) L_g = 9 mH and (**b**) L_g = 16 mH (**c**) FFT analysis of unstable current.

Figure 13 showcases the waveforms with the compensation method when R_v = 1, R_v = 2, R_v = 4. As depicted in Figure 13, the utilization of the compensation method reduces voltage and current distortion. Consequently, the studied system demonstrates stable operation with the utilization of the compensation method. Additionally, Figure 14 presents the fast Fourier transform (FFT) analysis of the current, indicating the damping of oscillation frequencies in all three cases.
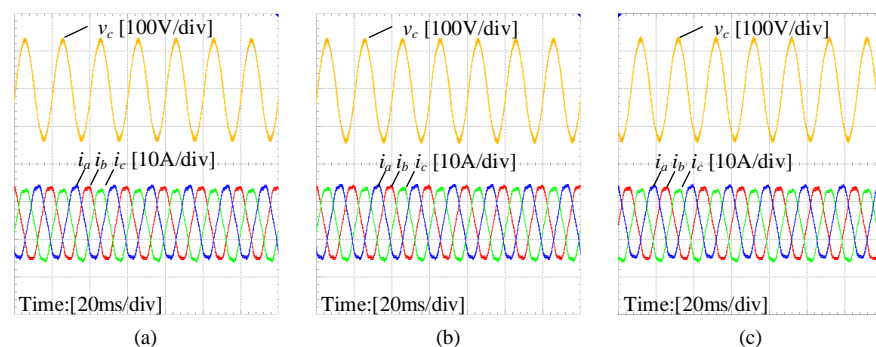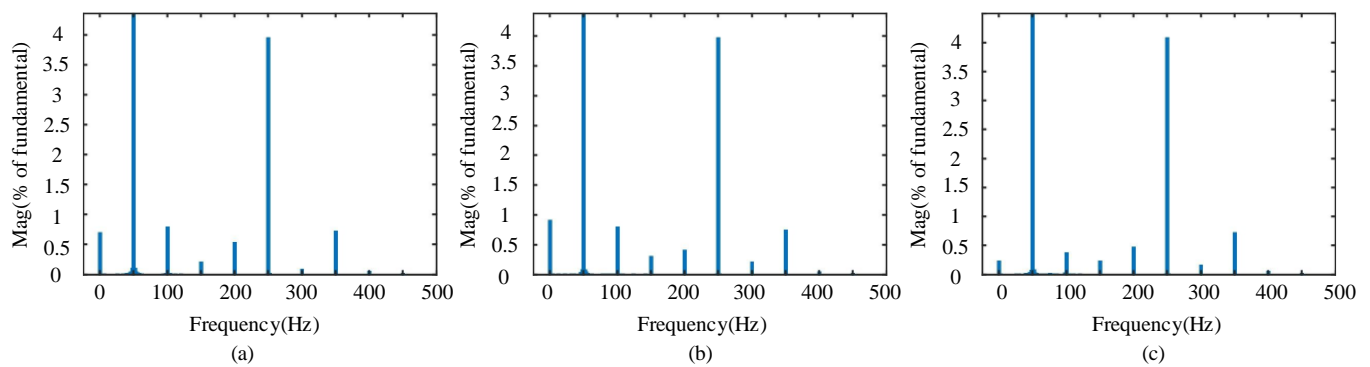

Figure 13. Waveforms with proposed compensation under (**a**) R_v = 1, (**b**) R_v = 2, and (**c**) R_v = 4.

Figure 14. FFT of current under Figure 13 (**a**) $R_v = 1$, (**b**) $R_v = 2$, and (**c**) $R_v = 4$.

Figure 15 exhibits the waveforms with the compensation method for $R_v = 2$ under case I. The parameter variations of the studied system alter the oscillation frequency. From Figure 15a, when the compensation is not utilized, the investigated system experiences resonance. When the compensation method is adopted, the resonance can be mitigated. But the reference of PLL will be changed. Thus, there is a transient current overshoot and reactive power before the phase lock process, as depicted in Figure 15c. Figure 16 shows the damping process of i_a, which is based on discrete Fourier transformation (DFT). The oscillation frequency of 16 Hz and 116 Hz will be attenuated after the adoption of the compensation method.
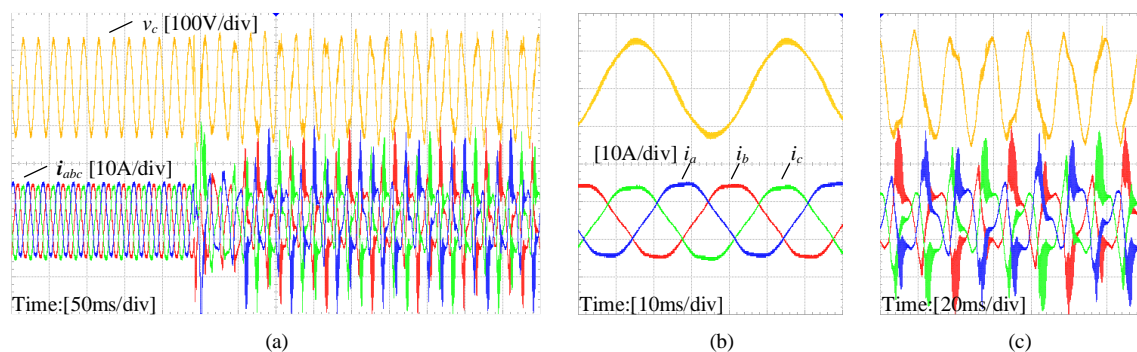

Figure 15. Case I (**a**) voltage and current waveforms (**b**) the stable waveforms (**c**) the unstable waveforms.
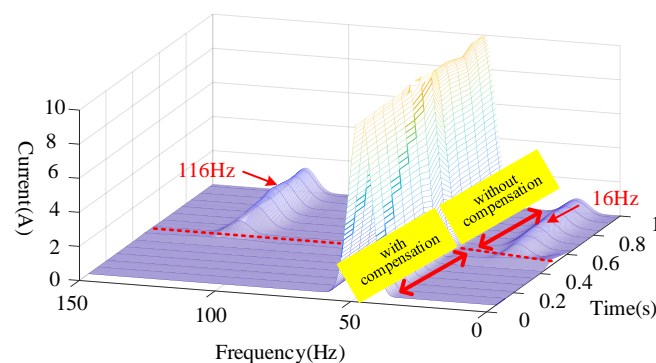

Figure 16. DFT of current under case I.

Figures 17 and 18 present the waveforms when $R_v = 2$ under case II and case III. It can be deduced that the compensation method effectively dampens the resonance even when the oscillation frequency has shifted, indicating the robustness of the method against the introduction of reactive power, fluctuations in PLL bandwidth, and grid impedance. These

experimental results provide further evidence of the effectiveness and robustness of the compensation method.
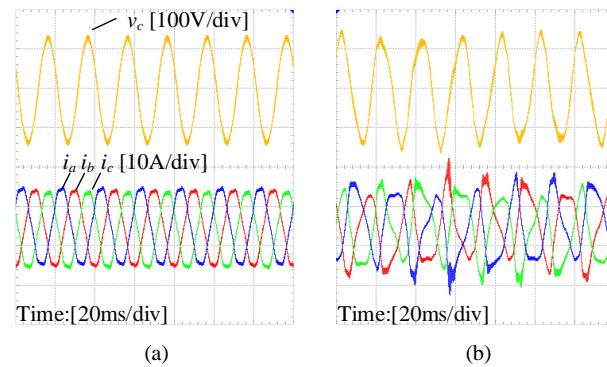
**Figure 17.** Case II. (**a**) The stable waveforms; (**b**) the unstable waveforms.
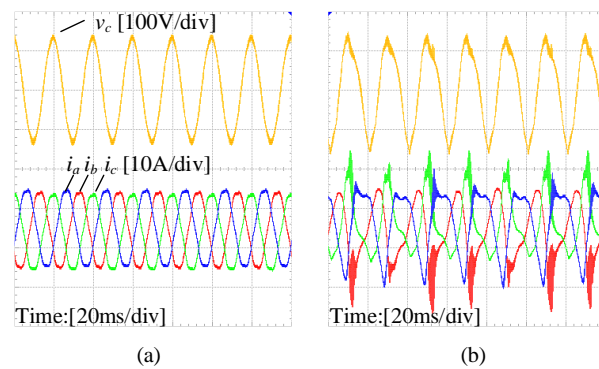
Figure 18. Case III. (**a**) The stable waveforms; (**b**) the unstable waveform.

Figure 19 illustrates the waveforms of when $R_v = 2$ under case IV and case V. Given Formula (23), the error in grid impedance measurement does not affect the effectiveness of the phase correction. In addition, the error of grid impedance measurement can be up to −70% and +160%, demonstrating the robustness of the compensation method to errors in grid impedance measurement, as verified experimentally.
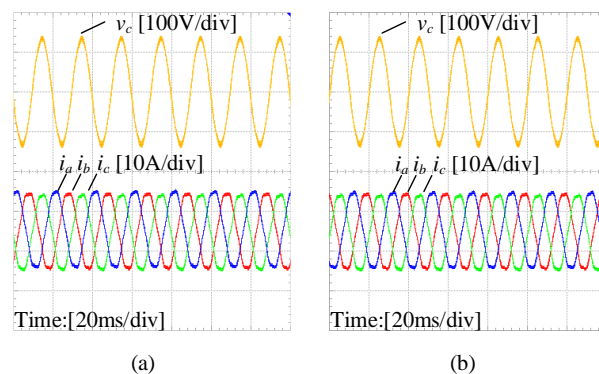
Figure 19. (**a**) The stable waveforms of case IV; (**b**) the stable waveforms of case V.

Moreover, the waveforms of when the frequency of the grid changes 0.5 Hz and −0.5 Hz and $R_v = 2$ are shown in Figure 20, which is conducted in MATLAB/Simulink. The system can maintain stability in both cases, which indicates the proposed compensation method can deal with the change of grid frequency.
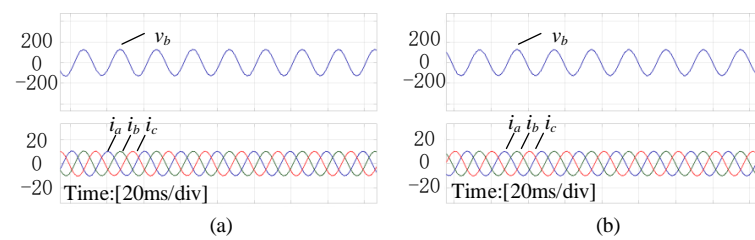
Figure 20. R_v = 2. (**a**) The waveforms of frequency changes 0.5 Hz; (**b**) the stable waveforms of frequency changes -0.5 Hz.

5. Conclusions and Future Work

This paper provides a clear exposition of the coupling mechanism in the grid-connected system. Based on this coupling mechanism, an equivalent parallel compensation method is proposed by altering the structure of PLL. This method introduces a virtual resistance in parallel with the grid impedance, which achieves the decouple of the studied system. It reshapes the inverter qq-axis impedance at the impedance level. By carefully designing the virtual resistance, the PLL dynamic performance can be maintained. Additionally, the method also has robustness to the parameter variations, such as the introduction of reactive power, the fluctuations of the PLL bandwidth, and grid impedance. And the error of grid impedance measurement can be up to -70% L_g and $+160\%$ L_g. Experimental waveforms further validate the effectiveness of this method.

The outlook of future work on this topic can be directed towards the following aspects:

(1) The instability mechanism of the grid-connected system can be deeply analyzed, which enables us to propose a more effective stability control method.
(2) The effectiveness and implementation of the equivalent parallel resistance compensation method in scenarios such as multiple inverters should be explored.

Author Contributions: Data curation, M.W., G.Y. and J.X.; formal analysis, M.W.; funding acquisition, J.Z. and J.L.; investigation, M.W. and G.Y.; methodology, M.W. and G.Y.; project administration, J.Z. and J.L.; resources, S.Y. and Y.Z.; software, M.W. and G.Y.; supervision, J.Z. and J.L.; validation, M.W., G.Y. and J.X.; visualization, M.W. and G.Y.; writing—original draft, M.W.; writing—review and editing, M.W., J.Z., G.Y., J.X. and J.L. All authors have read and agreed to the published version of the manuscript.

Data Availability Statement: Data are contained within the article.

Conflicts of Interest: Authors Shuangfei Yang, Yuebin Zhou were employed by the company China Southern Power Grid Co., Ltd. The remaining authors declare that the research was conducted in the absence of any commercial or financial relationships that could be construed as a potential conflict of interest.

References

1. Li, Y.; Fan, L.; Miao, Z. Stability Control for Wind in Weak Grids. *IEEE Trans. Sustain. Energy* **2019**, *10*, 2094–2103. [CrossRef]
2. Ma, J.; Shen, Y.; Du, Y.; Liu, H.; Wang, J. Overview on Active Damping Technology of Wind Power Integrated System Adapting to Broadband Oscillation. *Power Syst. Technol.* **2021**, *45*, 1673–1686. [CrossRef]
3. Sun, J. Impedance-Based Stability Criterion for Grid-Connected Inverters. *IEEE Trans. Power Electron.* **2011**, *26*, n3075–n3078. [CrossRef]
4. Wen, B.; Boroyevich, D.; Burgos, R.; Mattavelli, P.; Shen, Z. Analysis of D-Q Small-Signal Impedance of Grid-Tied Inverters. *IEEE Trans. Power Electron.* **2016**, *31*, 675–687. [CrossRef]
5. Tu, C.; Gao, J.; Xiao, F.; Guo, Q.; Jiang, F. Stability Analysis of the Grid-Connected Inverter Considering the Asymmetric Positive-Feedback Loops Introduced by the PLL in Weak Grids. *IEEE Trans. Ind. Electron.* **2022**, *69*, 5793–5802. [CrossRef]
6. Gong, H.; Wang, X.; Harnefors, L. Rethinking Current Controller Design for PLL-Synchronized VSCs in Weak Grids. *IEEE Trans. Power Electron.* **2021**, *37*, 1369–1381. [CrossRef]
7. Huang, L.; Xin, H.; Li, Z.; Ju, P.; Yuan, H.; Lan, Z.; Wang, Z. Grid-Synchronization Stability Analysis and Loop Shaping for PLL-Based Power Converters with Different Reactive Power Control. *IEEE Trans. Smart Grid* **2020**, *11*, 501–516. [CrossRef]

8. Wu, M.; Zeng, J.; Ying, G.; Liu, J. A d-axis current error compensation method based on coupling mechanism for Grid-Connected inverters under weak grid. *Int. J. Electr. Power Energy Syst.* **2023**, *151*, 109189. [CrossRef]
9. Shair, J.; Xie, X.; Li, H.; Zhao, W.; Liu, W. A grid-side multi-modal adaptive damping control of super-/sub-synchronous oscillations in type-4 wind farms connected to weak AC grid. *Electr. Power Syst. Res.* **2023**, *215*, 108963. [CrossRef]
10. Fang, J.; Li, X.; Li, H.; Tang, Y. Stability Improvement for Three-Phase Grid-Connected Converters through Impedance Reshaping in Quadrature-Axis. *IEEE Trans. Power Electron.* **2018**, *33*, 8365–8375. [CrossRef]
11. Li, G.; Chen, Y.; Luo, A.; Wang, Y. An Inertia Phase Locked Loop for Suppressing Sub-Synchronous Resonance of Renewable Energy Generation System under Weak Grid. *IEEE Trans. Power Syst.* **2021**, *36*, 4621–4631. [CrossRef]
12. Yang, D.; Wang, X.; Liu, F.; Xin, K.; Liu, Y.; Blaabjerg, F. Symmetrical PLL for SISO Impedance Modeling and Enhanced Stability in Weak Grids. *IEEE Trans. Power Electron.* **2020**, *35*, 1473–1483. [CrossRef]
13. Lin, X.; Wen, Y.; Yu, R.; Yu, J.; Wen, H. Improved Weak Grids Synchronization Unit for Passivity Enhancement of Grid-Connected Inverter. *IEEE J. Emerg. Sel. Top. Power Electron.* **2022**, *10*, 7084–7097. [CrossRef]
14. Tao, R.; Wu, M.; Ying, G.; Tang, J.; An, R.; Wang, Q.; Liu, J. A phase compensation method combined with power correction for suppressing sub-synchronous resonance of wind generation under weak grid. *Int. J. Electr. Power Energy Syst.* **2023**, *151*, 109115. [CrossRef]
15. Li, C.; Liu, W.; Liang, J.; Ding, X.; Cipcigan, L.M. Improved Grid Impedance Compensation for Phase-Locked Loop to Stabilize the Very-Weak-Grid Connection of VSIs. *IEEE Trans. Power Deliv.* **2022**, *37*, 3863–3872. [CrossRef]
16. Duan, Z.; Meng, Y.; Wu, K.; Yang, Y.; Wang, X.; Wang, X. Back-electromotive-force observer (BEMF observer) based symmetrical PLL for grid synchronization stability enhancement under weak grid conditions. *IET Gener. Transm. Distrib.* **2022**, *16*, 4068–4079. [CrossRef]
17. Mirmohammad, M.; Azad, S.P. Control and Stability of Grid-Forming Inverters: A Comprehensive Review. *Energies* **2024**, *17*, 3186. [CrossRef]
18. Gui, Y.; Wang, X.; Blaabjerg, F. Vector Current Control Derived from Direct Power Control for Grid-Connected Inverters. *IEEE Trans. Power Electron.* **2019**, *34*, 9224–9235. [CrossRef]
19. Gui, Y.; Wang, X.; Wu, H.; Blaabjerg, F. Voltage-Modulated Direct Power Control for a Weak Grid-Connected Voltage Source Inverters. *IEEE Trans. Power Electron.* **2019**, *34*, 11383–11395. [CrossRef]
20. Li, M.; Zhang, X.; Yang, Y.; Cao, P. The Grid Impedance Adaptation Dual Mode Control Strategy in Weak Grid. In Proceedings of the 2018 International Power Electronics Conference (IPEC-Niigata 2018-ECCE Asia), Niigata, Japan, 20–24 May 2018; pp. 2973–2979. [CrossRef]
21. Wang, S.; Cui, K.; Hao, P. Grid-Connected Inverter Grid Voltage Feedforward Control Strategy Based on Multi-Objective Constraint in Weak Grid. *Energies* **2024**, *17*, 3288. [CrossRef]
22. Zhu, D.; Zhou, S.; Zou, X.; Kang, Y. Improved Design of PLL Controller for *LCL*-Type Grid-Connected Converter in Weak Grid. *IEEE Trans. Power Electron.* **2020**, *35*, 4715–4727. [CrossRef]
23. Li, X.; Lin, H. A Design Method of Phase-Locked Loop for Grid-Connected Converters Considering the Influence of Current Loops in Weak Grid. *IEEE J. Emerg. Sel. Top. Power Electron.* **2020**, *8*, 2420–2429. [CrossRef]
24. Li, Y.; Chen, J.; Wang, X.; Zhang, X.; Zhao, X. Dynamic Stability Study of Grid-Connected Inverter Based on Virtual Synchronizer under Weak Grid. *Energies* **2022**, *15*, 7091. [CrossRef]
25. Piyasinghe, L.; Miao, Z.; Khazaei, J.; Fan, L. Impedance Model-Based SSR Analysis for TCSC Compensated Type-3 Wind Energy Delivery Systems. *IEEE Trans. Sustain. Energy* **2015**, *6*, 179–187. [CrossRef]
26. Wang, X.; Harnefors, L.; Blaabjerg, F. Unified Impedance Model of Grid-Connected Voltage-Source Converters. *IEEE Trans. Power Electron.* **2018**, *33*, 1775–1787. [CrossRef]
27. Lin, X.; Yu, J.; Yu, R.; Zhang, J.; Yan, Z.; Wen, H. Improving Small-Signal Stability of Grid-Connected Inverter Under Weak Grid by Decoupling Phase-Lock Loop and Grid Impedance. *IEEE Trans. Ind. Electron.* **2022**, *69*, 7040–7053. [CrossRef]